AIAA 2000-4323

Recent Turbulence Model Advances Applied to Multielement Airfoil Computations

Christopher L. Rumsey and
Thomas B. Gatski
NASA Langley Research Center
Hampton, Virginia

18th Applied Aerodynamics Meeting
14-17 August 2000/Denver, CO

AIAA-2000-4323

RECENT TURBULENCE MODEL ADVANCES APPLIED TO MULTIELEMENT AIRFOIL COMPUTATIONS

Christopher L. Rumsey* and Thomas B. Gatski†
NASA Langley Research Center
Hampton, Virginia

Abstract

A one-equation linear turbulence model and a two-equation nonlinear explicit algebraic stress model (EASM) are applied to the flow over a multielement airfoil. The effect of the K-ε and K-ω forms of the two-equation model are explored, and the K-ε form is shown to be deficient in the wall-bounded regions of adverse pressure gradient flows. A new K-ω form of EASM is introduced. Nonlinear terms present in EASM are shown to improve predictions of turbulent shear stress behind the trailing edge of the main element and near midflap. Curvature corrections are applied to both the one- and two-equation turbulence models and yield only relatively small local differences in the flap region, where the flow field undergoes the greatest curvature. Predictions of maximum lift are essentially unaffected by the turbulence model variations studied.

1 Introduction

In recent studies,[1,2] analyses of high-lift multielement airfoil configurations were performed to assess the predictive capability of turbulence models. These studies were undertaken in part to determine why, in comparison with nominally two-dimensional (2-D) experiments, CFD overpredicts maximum lift and the angle at which maximum lift occurs. In general, with the full airfoil configuration, it is difficult to isolate the deficiencies of turbulence models. However, the studies revealed three areas where turbulence model predictions were *possibly* deficient and could adversely affect the overall prediction of the flow field. These areas were (1) prediction of transition location, (2) prediction of downstream evolution of the slat wake, and (3) accounting for streamwise curvature effects in the flap region. Additional studies over the last several years have examined some of these possible modeling deficiencies in isolation by using "unit problems." Section 2 highlights results from these studies.

The current study was an effort to gauge the effects of recent turbulence model advances (some of which resulted from unit problem investigations) on a multielement airfoil near maximum lift. The study investigated three major areas: the effects of K-ε vs. K-ω formulations, the effects of nonlinear terms, and the effects of curvature corrections. Following section 3, in which the numerical method and turbulence models are briefly described, the three major areas are discussed in turn in section 4. For all results in this paper, we have focused our attention on the region of the configuration near the main element trailing edge and flap, where previous studies have shown the greatest discrepancies with experimental data.

2 Summary of Unit Problem Investigations

Rumsey et al.[3] investigated the ability of three turbulence models to model the effects of convex curvature in a U-duct unit problem. In particular, convex curvature is known to cause a suppression of the turbulent shear stress in the outer part of the boundary layer. The three turbulence models — one-equation Spalart-Allmaras (SA),[4] two-equation Menter shear-stress transport (SST),[5] and two-equation explicit algebraic stress model (EASM)[6] — all behaved similarly in the curved region, and all failed to predict the suppression of the turbulent shear stress. It was shown that a Reynolds stress model (RSM) can predict the suppression, and that the source of the error in EASM (which is derived directly from RSM) is the assumption of anisotropy equilibrium in the Cartesian frame of reference:

$$\frac{Db_{ij}}{Dt} = 0, \qquad (1)$$

*Senior Research Scientist, Computational Modeling and Simulation Branch, Associate Fellow AIAA.

†Senior Research Scientist, Computational Modeling and Simulation Branch.

where $b_{ij} = [\tau_{ij}/(2K)] - (\delta_{ij}/3)$ and where $K = \tau_{nn}/2$ is the turbulent kinetic energy.

Gatski and Rumsey[7] showed that by assuming Eq. (1) to hold, not in the Cartesian frame but rather in the frame defined by the principal axes of the strain rate tensor, a new form of the EASM could be derived that takes into account the flow field curvature. With the new EASM curvature-corrected (EASMCC) method, the suppression of the turbulent shear stress near the convex bend of the U-duct was accurately predicted.[8]

A curvature correction for the SA model has also been developed by Spalart and Shur[9] and applied to the same U-duct flow in Shur et al.[10] This correction, Spalart-Allmaras for rotation and curvature (SARC) is based similarly on the rate of change of the principal axes of the strain rate tensor, but it also includes a heuristic function f_{r1} (that multiplies the model's production term) not present in the EASMCC.

A different unit problem of wake development in various pressure gradients (an experiment conducted by Liu et al.[11]) was investigated by Carlson et al.[12] This unit problem was motivated by the fact that most turbulence models have overpredicted the slat wake depth and width on the multielement airfoil, even when transition is specified according to experimental measurements.[13] Using a linear two-equation eddy viscosity model and EASM, Carlson et al. showed that the isolated effects of pressure gradient on near-wake mean flow development could be reasonably predicted by both turbulence models; results compared favorably with the experiment.

However, the pressure gradients experienced by the slat wake in the real multielement configuration are highly variable (a short, very strong favorable gradient followed by a longer adverse gradient), and these gradients can be significantly stronger than those imposed in the unit problem experiment (which had constant $\partial p/\partial x$). Therefore, it is still not known whether (1) the stronger (or variable) pressure gradients in the multielement wake cause a failure of the turbulence models, or (2) the turbulence models are not to blame and some other effects not being modeled in the CFD, such as unsteadiness or three-dimensional (3-D) effects, are causing the discrepancy.

Finally, on-going separate work is focusing on transition prediction within the context of the EASM, based on rigorous mathematical treatment.[14,15] However, this effort is quite complex and longer term. A shorter term, empirically based method for predicting transition within a two-equation turbulence model has been applied to the multielement configuration by Czerwiec et al.[16]

3 Numerical Method and Turbulence Models

The CFD code used in the current investigation was CFL3D,[17] a widely used structured-grid upwind finite-volume method. Details about the code can be found in the user's manual referenced.

Of the three fundamental investigations described in this paper, the first is the effects of the K-ε vs. K-ω underlying formulation for the EASM turbulence model. Two versions of the EASM are denoted by EASM(K-ε) and EASM(K-ω), respectively. The EASM(K-ω) is described in detail in the appendix, whereas the EASM(K-ε) has been described previously in Ref. 3 and will not be repeated here. However, note that the EASM(K-ε) has an additional minor modification, described by Gatski and Rumsey,[7] in order to correct for a tendency of the original model to produce excessive levels of eddy viscosity near the center of wakes; these excessive levels result in a nonphysical, local "flattening" of the velocity profiles. Equation (4) in Ref. 3 has been replaced by

$$g = \left[\gamma_0^* \frac{\mathcal{P}}{\varepsilon} + \gamma_1^*\right]^{-1}, \tag{2}$$

where

$$\gamma_0^* = \gamma_0 - 1 \tag{3}$$

and

$$\gamma_1^* = \gamma_1 + 1 + \left(\frac{C_{\varepsilon 2} - C_{\varepsilon 1}}{C_{\varepsilon 1} - 1}\right). \tag{4}$$

This modification only slightly affects results for the log layer, where C_μ (Eq. (29) of Ref. 3) now requires the value of 0.0885 for EASM(K-ε). The EASM(K-ω) described in the appendix also includes the above modifications to g $(= a_4/\tau)$.

The second fundamental investigation described is the effects of the nonlinear terms themselves. In EASM, the turbulent stress tensor is not only a function of the strain rate, but of two additional nonlinear terms as well (see the appendix). For this part of the study, we used the EASM(K-ω) with and without its nonlinear terms in place.

The third fundamental investigation is an exploration of the effects of curvature on the multielement airfoil case considered. Four turbulence models were employed for this part of the study: SA, SARC, EASM(K-ω), and EASMCC(K-ω) (in other words, SA and EASM(K-ω) with and without their respective curvature corrections).

Brief descriptions of the curvature corrections for SARC and EASMCC are given here. Both use the

kinematic strain rate and rotation rate tensors, S_{ij} and W_{ij} respectively, defined in the appendix. These corrections are similar in that they both employ the Lagrangian derivative of the strain-tensor principal axes, given by

$$\frac{D\alpha}{Dt} = \frac{1}{2(S_{11}^2 + S_{12}^2)} \left[S_{11} \frac{DS_{12}}{Dt} - S_{12} \frac{DS_{11}}{Dt} \right]. \quad (5)$$

However, the two curvature corrections were developed independently and are different in many other respects.

In the current implementation of the SARC model, a portion of the SA model's production term, $c_{b1}[1 - f_{t2}]W\tilde{\nu}$, was replaced by $c_{b1}[f_{r1} - f_{t2}]W\tilde{\nu}$, where

$$f_{r1} = (1 + c_{r1}) \frac{2r^*}{(1 + r^*)} \left[1 - c_{r3} \tan^{-1}(c_{r2}\tilde{r}) \right] - c_{r1}, \quad (6)$$

and $c_{r1} = 1, c_{r2} = 12$. The constant c_{r3} was assigned to be both 1.0 and 0.6 in Spalart and Shur,[9] who admitted they are still experimenting with the heuristic function f_{r1}. For the current study, we used $c_{r3} = 0.6$. The function r^* is given by $r^* = S/W$, where $S = \sqrt{2S_{ij}S_{ij}}$ and $W = \sqrt{2W_{ij}W_{ij}}$. For 2-D flows and no system rotation, the expression for $\tilde{r}$ in Ref. 10 can be reduced to

$$\tilde{r} = -\left(\frac{D\alpha}{Dt} \right) \frac{8W_{12} \left(S_{11}^2 + S_{12}^2 \right)}{D^4}, \quad (7)$$

where $D\alpha/Dt$ is given by Eq. (5) and $D = \sqrt{0.5(S^2 + W^2)}$.

In the study of non-Newtonian constitutive relations (e.g., Schunk and Scriven,[18] Souza Mendes et al.[19]), a measure of relative rotation rate is based on the principal axes of the strain rate tensor. As mentioned in the introduction, Gatski and Rumsey[7] used this measure to derive EASMCC, which takes into account the flow field curvature.

The method for implementation of EASMCC in 2-D is as follows. The rotation rate tensor W_{ij} in the model is replaced by $W_{ij} - \Omega_{ij}/a_2$, where the constant a_2 is defined by the pressure-strain correlation model (recall that $W_{ij} - \Omega_{ij}$ is the absolute rotation rate tensor). For the SSG model[20] used here, $a_2 = (2 - C_4)/2$ and $C_4 = 0.4$. The tensor Ω_{ij} is given by

$$\Omega_{ij} = \begin{bmatrix} 0 & D\alpha/Dt \\ -D\alpha/Dt & 0 \end{bmatrix}, \quad (8)$$

and $D\alpha/Dt$ is given by Eq. (5).

4 Results

In the current study we focused primarily on the region of the flow field in the vicinity from the main element trailing edge to the midflap area. This region was identified by Ying et al.[2] as an area where CFD results generally differ substantially from experimental data. It is also the region where any streamwise curvature effects would be expected, because the flow turns rapidly through 30–40 deg as it passes over the flap. A diagram showing the 30P-30N multielement configuration is shown in Fig. 1, with the current region of focus delineated.

Unless otherwise noted, all computations shown were performed on a "free-air" grid at $\alpha = 19$ deg, $M = 0.2$, and Re = 9 million. The effect of modeling the lower and upper tunnel walls in the CFD grid was explored in Ref. 21 and is not repeated here. Also, grid effects have been studied previously for this configuration (see discussion on numerical sensitivity in Rumsey et al.[1]); the current 4-zone grid contains 135,428 grid points. The transition locations on each element were specified at the end of the measured ranges given in Ref. 13.

4.1 Effects of ε vs. ω Formulations

The EASM model can be coupled with any two-equation model formulation; in this study, we explored the effects of K-ε vs. K-ω. Velocity profiles are shown in Fig. 2 at $x/c = 0.85$, near the trailing edge of the main element upper surface. In the plot, d refers to the normal distance from the airfoil surface and c is the *stowed* chord length. Results from using EASM(K-ω) showed better agreement with the main element boundary layer thickness and slat wake depth than results with EASM(K-ε). Although not shown, the latter model overpredicted the turbulence levels in the wall-bounded adverse pressure gradient regions over both the slat and the main element. This overprediction caused thicker predicted boundary layers, and consequently wakes too wide and deep.

The inability of K-ε models in general to handle wall-bounded adverse pressure gradients is a known problem characteristic of the ε-equation. See, for example, Wilcox,[22] Rodi and Scheuerer,[23] and Nagano and Tagawa.[24] In Ref. 23, the shortcomings are examined and it is shown that the generation term of the ε-equation has to be increased.

Figure 3 shows a plot of the predicted velocities in wall variables as compared to Spalding theory[25] at $x/c = 0.85$. The EASM(K-ε) did not obtain the correct slope of the log layer in this adverse pressure gradient flow. (Although not shown, EASM(K-ε), like other K-ε models, per-

forms well for wall-bounded, zero-pressure-gradient flows.) EASM(K-ω) had no trouble handling the adverse-pressure-gradient flow, and obtained the correct log-layer slope and position.

From these results, it appears clear that EASM(K-ε) should not be used for flow fields of the type explored in this study. (For that matter, *any* K-ε model without a modification, e.g. Ref. 23, probably cannot correctly predict wall-bounded adverse pressure gradients flows.) Therefore, for all results in the remainder of the paper, only the EASM(K-ω) version of EASM was used. For brevity, EASM(K-ω) and EASMCC(K-ω) models will henceforth be referred to as EASM and EASMCC, respectively.

4.2 Effects of Nonlinear Terms

Figure 4 shows experimentally measured[26] turbulent shear stresses at $x/c = 0.85$ near the trailing edge of the main element and at $x/c = 0.898$ on the flap. In the figure, the latter curve has been shifted to align the relevant features. The experiment indicated almost no change in the minimum $\overline{u'v'}$ level (near $d/c = 0.01$) between these two nearby locations. On the other hand, the SA model predicted a large change in the turbulent shear stress as the flow passed from the trailing edge to the wake, as shown in Fig. 5. Ying et al.[2] surmised that the reason for this too-rapid change was due to the Boussinesq eddy-viscosity assumption inherent in the SA (and other linear models). In the Boussinesq assumption, the turbulent shear stress is assumed to be directly proportional to the strain, so that $\tau_{ij} = -2\nu_t S_{ij}$. In this flow field, as the strain rate changes rapidly from the trailing edge to the wake, so too does the turbulent shear stress because ν_t from the SA varies smoothly and gradually there.

In contrast, the EASM (Fig. 6) did a better job maintaining the minimum shear stress level between these two stations. But what was the role of the nonlinear terms in the improved predictions? This question was investigated by solving EASM as a linear eddy viscosity model (i.e., by forcing the nonlinear terms to be zero). Results, shown in Fig. 7, indicate a large difference from the results of Fig. 6. Thus, the nonlinear terms appear to be necessary to capture more closely the streamwise development of the turbulent shear stress in this region.

4.3 Effects of Curvature Correction

The curvature correction for EASMCC encountered some numerical difficulties for this case, associated primarily with the explicit one-to-one interfaces in the wake-cut regions of the C-grids. Near the connectivity interfaces, small discontinuities could result in large levels of DS_{ij}/Dt, which would feed back into the solution through Ω_{ij} and worsen the discontinuities. To remove this problem, the curvature terms were turned on only in regions of the grid that contain a wall at the $k = 1$ index location. Furthermore, the velocities used in the determination of DS_{ij}/Dt were smoothed by using 10 iterations of an explicit point Gauss-Seidel Laplacian smoother,[27] and the elements of the Ω_{ij} matrix were limited to prevent unreasonably large levels from occurring. Note that these numerical difficulties did not occur with EASMCC for simpler (e.g., single-zone grid) cases.[7] Because of the smooth limiting inherent in the $\tan^{-1}$ function in the empirical f_{r1} expression, SARC did not encounter any numerical difficulties for this case.

Velocity profiles from the four turbulence models are shown at three stations, from the trailing edge of the main element to the middle of the flap, in Figs. 8–10. The corresponding turbulent shear stress profiles are shown in Figs. 11–13, respectively. We note five items of interest in these figures. (1) In general, all turbulence models produced very similar velocity profiles at each of the stations; the slat wake was (as expected) predicted to be too wide and too deep, although SARC decreased the wake depth slightly. Many other features of the experimental profiles were captured extremely well by all models. (2) The EASMCC overpredicted the magnitude of $\overline{u'v'}$ near $d/c = 0.01$ in Fig. 11; however, this overprediction is believed to be due to the use of the Laplacian smoother so near to a region of high S_{ij} gradient. (3) All models underpredicted the peak $\overline{u'v'}$ near $d/c = 0.02$ at midflap (Fig. 13). (4) Both SARC and EASMCC predicted some local differences in $\overline{u'v'}$ levels, but the curvature corrections overall had relatively minor effects. (5) As noted earlier, the EASM did a better job predicting the turbulent shear stress just downstream of the main element trailing edge ($x/c = 0.898$); the EASM also did a better job predicting the same quantity in the region of the upper half of the main wake (near $d/c = 0.04$) at midflap (Fig. 13). It was previously thought that poor prediction by the SA model here possibly was due to the model's inability to account for curvature effects. However, SARC's curvature correction did not have much impact. As shown in Fig. 14, the *nonlinear terms* appear to have the most influence on the $\overline{u'v'}$ levels in the midflap area.

4.4 Global Effects near Maximum Lift

Clearly, many of the discrepancies in turbulent shear stress between previous CFD results[2] and experiment in the current region of focus were due

to use of the Boussinesq eddy viscosity hypothesis. Nonetheless, these discrepancies appear to have little effect on the velocity profiles in this region: EASM yielded generally improved turbulent shear stress predictions over the flap, but in spite of this improvement, the model did no better overall than SA in the prediction of mean velocity. Curvature corrections in both the one-equation and two-equation models had a relatively minor effect for this flow. However, the fact that the SARC decreased the depth of the slat wake is intriguing and merits more detailed study.

One important question remains to be answered. Recalling past studies (e.g., Ref. 28) where, compared with nominally 2-D experiments, CFD overpredicted maximum lift, we now ask whether any of the turbulence model improvements described in this paper improve the global comparisons. Figure 15 shows results for SA, SARC, and EASM at angles of attack beyond $\alpha = 19$ deg. The EASMCC was not run for these cases. As in the past studies, all three models yielded higher C_ℓ levels and a higher stall angle ($\alpha = 23$ deg) than experiment ($\alpha = 21$ deg). In other words, improved turbulence shear stress predictions of EASM had little effect on CFD global force results near maximum lift. Curvature correction terms in SARC also had little effect. The reason for CFD's overprediction of maximum lift levels remains unknown. However, results from this study support the conclusion from an earlier study[1] that turbulence modeling is probably *not* the primary cause for the disagreement. A more likely cause is 3-D effects at high angles of attack in the wind tunnel; such effects are obviously not modeled by 2-D CFD.

5 Summary

Several turbulence model improvements, developed from unit problem investigations, were incorporated into a study of the flow over the 30P-30N multielement airfoil. As a result, turbulent shear stress prediction capabilities have been improved, and the influence of certain turbulence model components has been established. The K-ε form of the EASM was shown to be ill suited for use in this flow field because it overpredicts turbulence in regions of adverse-pressure-gradient wall-bounded flow. This problem is inherent in the "standard" form of the K-ε equations; the K-ω form does not suffer from this problem. A new K-ω form of the EASM was introduced. Nonlinear terms, present in the EASM, were shown to improve the prediction of the turbulent shear stress behavior behind the trailing edge of the main element and near midflap, but these improvements had little effect on the mean flow field. Finally, curvature corrections in two different models were applied to this flow field. Overall, these corrections did not have a significant effect in the flap region, where the flow field undergoes the greatest curvature. Predictions of maximum lift were essentially unaffected by the turbulence model variations studied.

References

1. Rumsey, C. L., Gatski, T. B., Ying, S. X., and Bertulrud, A., "Prediction of High-Lift Flows Using Turbulent Closure Models," *AIAA Journal*, Vol. 36, No. 5, 1998, pp. 765–774.

2. Ying, S. X., Spaid, F. W., McGinley, C. B., and Rumsey, C. L., "Investigation of Confluent Boundary Layers in High-Lift Flows," *Journal of Aircraft*, Vol. 36, No. 3, 1999, pp. 550–562.

3. Rumsey, C. L., Gatski, T. B., and Morrison, J. H., "Turbulence Model Predictions of Extra-Strain Rate Effects in Strongly-Curved Flows," AIAA Paper 99-0157, Jan. 1999.

4. Spalart, P. R., and Allmaras, S. R., "A One-Equation Turbulence Model for Aerodynamic Flows," *La Recherche Aerospatiale*, No. 1, 1994, pp. 5–21.

5. Menter, F. R., "Improved Two-Equation K-ω Turbulence Models for Aerodynamic Flows," NASA TM 103975, Oct. 1992.

6. Gatski, T. B., and Speziale, C. G., "On Explicit Algebraic Stress Models for Complex Turbulent Flows," *Journal of Fluid Mechanics*, Vol. 254, 1993, pp. 59–78.

7. Gatski, T. B., and Rumsey, C. L., "Linear and Non-Linear Eddy Viscosity Models," *Closure Strategies for Turbulent and Transitional Flows*, edited by B. E. Launder and N. D. Sandham, Cambridge University Press, to appear 2000.

8. Rumsey, C. L., Gatski, T. B., and Morrison, J. H., "Turbulence Model Predictions of Strongly-Curved Flow in a U-Duct," *AIAA Journal*, to appear 2000.

9. Spalart, P. R., and Shur, M. L., "On the Sensitization of Turbulence Models to Rotation and Curvature," *Aerospace Science and Technology*, No. 5, 1997, pp. 297–302.

10. Shur, M. L., Strelets, M. K., Travin, A. K., and Spalart, P. R., "Turbulence Modeling in

Rotating and Curved Channels: Assessing the Spalart-Shur Correction," *AIAA Journal*, Vol. 38, No. 5, 2000, pp. 784–792.

11. Liu, X., Thomas, F. O., and Nelson, R. C., "An Experimental Investigation of Wake Development in Arbitrary Pressure Gradient," AIAA Paper 99-0677, Jan. 1999.

12. Carlson, J. R., Duquesne, N., Rumsey, C. L., and Gatski, T. B., "Computation of Turbulent Wake Flows in Variable Pressure Gradient," *Computers and Fluids*, to appear 2000.

13. Bertelrud, A., "Use of Empirical Transition Correlations for Flow Around High-Lift Configurations," AIAA Paper 99-0541, Jan. 1999.

14. Thacker, W. D., Gatski, T. B., and Grosch, C. E., "Analyzing Mean Transport Equations of Turbulence and Linear Disturbances in Decaying Flows," *Physics of Fluids*, Vol. 11, No. 9, 1999, pp. 2626–2631.

15. Thacker, W. D., Grosch, C. E., and Gatski, T. B., "Modeling the Dynamics of Ensemble-Averaged Linear Disturbances in Homogeneous Shear Flow," *Journal of Flow, Turbulence, and Combustion*, to appear 2000.

16. Czerwiec, R., Edwards, J. R., Rumsey, C. L., and Hassan, H. A., "Theory and Experiment of Multielement Airfoils - A Comparison," AIAA Paper 2000-0984, Jan. 2000.

17. Krist, S. L., Biedron, R. T., and Rumsey, C. L., "CFL3D User's Manual (Version 5.0)," NASA TM-1998-208444, June 1998.

18. Schunk, P. R., and Scriven, L. E., "Constitutive Equation for Modeling Mixed Extension and Shear in Polymer Solution Processing," *Journal of Rheology*, Vol. 34, 1990, pp. 1085–1119.

19. Souza Mendes, P. R., Padmanabhan, M., Scriven, L. E., and Macosko, C. W., "Inelastic Constitutive Equations for Complex Flows," *Rheological Acta*, Vol. 34, 1995, pp. 209–214.

20. Speziale, C. G., Sarkar, S., and Gatski, T. B., "Modeling the Pressure-Strain Correlation of Turbulence: an Invariant Dynamical Systems Approach," *Journal of Fluid Mechanics*, Vol. 227, 1991, pp. 245–272.

21. Rumsey, C. L., Gatski, T. B., Ying, S. X., and Bertulrud, A., "Prediction of High-Lift Flows Using Turbulent Closure Models," AIAA Paper 97-2260, June 1997.

22. Wilcox, D. W., *Turbulence Modeling For CFD*, 2nd ed., DCW Industries, La Canada, 1998.

23. Rodi, W., and Scheuerer, G., "Scrutinizing the K-ε Turbulence Model Under Adverse Pressure Gradient Conditions," *Journal of Fluids Engineering*, Vol. 108, No. 6, 1986, pp. 174–179.

24. Nagano, Y., and Tagawa, M., "An Improved K-ε Model for Boundary Layer Flows," *Journal of Fluids Engineering*, Vol. 112, No. 3, 1990, pp. 33–39.

25. White, F. M., *Viscous Fluid Flow*, McGraw-Hill Book Company, New York, 1974, p. 475.

26. McGinley, C. B., Anders, J. B., and Spaid, F. W., "Measurements of Reynolds Stress Profiles on a High-Lift Airfoil," AIAA Paper 98-2620, June 1998.

27. Hirsch, C., *Numerical Computation of Internal and External Flows*, Vol. 1, John Wiley & Sons, Chichester, 1992, p. 462.

28. Anderson, W. K., Bonhaus, D. L., McGhee, R. J., and Walker, B. S., "Navier-Stokes Computations and Experimental Comparisons for Multielement Airfoil Configurations," *Journal of Aircraft*, Vol. 32, No. 6, 1995, pp. 1246–1253.

29. Gatski, T. B., "Turbulent Flows: Model Equations and Solution Methodology," *Handbook of Computational Fluid Mechanics*, edited by R. Peyret, Academic Press, London, 1996, pp. 339–415.

30. Jongen, T., and Gatski, T. B., "A Unified Analysis of Planar Homogeneous Turbulence Using Single-Point Closure Equations," *Journal of Fluid Mechanics*, Vol. 399, 1999, pp. 117–150.

Appendix

This appendix explicitly defines the EASM(K-ω) turbulence model, for readers interested in coding it themselves. For details on the *derivation* of the EASM, the reader is referred to earlier papers on EASM listed in the references.

The turbulent stress tensor for EASM is given by

$$\begin{aligned}\tau_{ij} = \quad & \frac{2}{3}K\delta_{ij} - 2\nu_t^*\Big(S_{ij} \\ & +\big[a_2a_4(S_{ik}W_{kj} - W_{ik}S_{kj}) \\ & -2a_3a_4\big(S_{ik}S_{kj} - \frac{1}{3}S_{kl}S_{lk}\delta_{ij}\big)\big]\Big), \qquad (9)\end{aligned}$$

where $S_{ij} = [(\partial u_i/\partial x_j) + (\partial u_j/\partial x_i)]/2$ and $W_{ij} = [(\partial u_i/\partial x_j) - (\partial u_j/\partial x_i)]/2$. The nonlinear terms are

within the brackets [ ]. The component τ_{ij} terms are used to close the Reynolds-averaged Navier-Stokes equations (see, e.g., Ref. 29). The kinematic eddy viscosity ν_t^* is given by

$$\nu_t^* \equiv C_\mu^* K\tau = -K\alpha_1, \tag{10}$$

with $\tau \equiv 1/\omega$. Thus, α_1/τ is equivalent to $-C_\mu^*$. The value of α_1/τ is obtained from the solution to the following cubic equation at each point in the flow field:

$$\left(\frac{\alpha_1}{\tau}\right)^3 + p\left(\frac{\alpha_1}{\tau}\right)^2 + q\left(\frac{\alpha_1}{\tau}\right) + r = 0, \tag{11}$$

where

$$p = -\frac{\gamma_1^*}{\eta^2\tau^2\gamma_0^*} \tag{12}$$

$$q = \frac{1}{(2\eta^2\tau^2\gamma_0^*)^2}\Big(\gamma_1^{*2} - 2\eta^2\tau^2\gamma_0^* a_1 - \frac{2}{3}\eta^2\tau^2 a_3^2 + 2\mathcal{R}^2\eta^2\tau^2 a_2^2\Big) \tag{13}$$

$$r = \frac{\gamma_1^* a_1}{(2\eta^2\tau^2\gamma_0^*)^2}. \tag{14}$$

The correct root to choose from this equation is the root with the lowest real part.[30] Also, the degenerate case when $\eta^2 \to 0$ must be avoided. The current solution procedure used is as follows:

If $\eta^2\tau^2 < 1 \times 10^{-6}$, then

$$\left(\frac{\alpha_1}{\tau}\right) = -\frac{\gamma_1^* a_1}{\gamma_1^{*2} - 2\{\mathbf{W}^2\}\tau^2 a_2^2}. \tag{15}$$

Otherwise, define

$$a \equiv q - \frac{p^2}{3} \tag{16}$$

$$b \equiv \frac{1}{27}(2p^3 - 9pq + 27r) \tag{17}$$

$$d \equiv \frac{b^2}{4} + \frac{a^3}{27}. \tag{18}$$

Then, if $d > 0$

$$t_1 = \left(-\frac{b}{2} + \sqrt{d}\right)^{1/3} \tag{19}$$

$$t_2 = \left(-\frac{b}{2} - \sqrt{d}\right)^{1/3} \tag{20}$$

$$\left(\frac{\alpha_1}{\tau}\right) = \min\left(-\frac{p}{3} + t_1 + t_2, -\frac{p}{3} - \frac{t_1}{2} - \frac{t_2}{2}\right) \tag{21}$$

If $d \le 0$, then

$$\theta = \cos^{-1}\left(-\frac{b}{2}\Big/\sqrt{-\frac{a^3}{27}}\right) \tag{22}$$

$$t_1 = -\frac{p}{3} + 2\sqrt{-\frac{a}{3}}\cos\left(\frac{\theta}{3}\right) \tag{23}$$

$$t_2 = -\frac{p}{3} + 2\sqrt{-\frac{a}{3}}\cos\left(\frac{2\pi}{3} + \frac{\theta}{3}\right) \tag{24}$$

$$t_3 = -\frac{p}{3} + 2\sqrt{-\frac{a}{3}}\cos\left(\frac{4\pi}{3} + \frac{\theta}{3}\right) \tag{25}$$

$$\left(\frac{\alpha_1}{\tau}\right) = \min\left(t_1, t_2, t_3\right). \tag{26}$$

In the current implementation, the resulting $C_\mu^* = -(\alpha_1/\tau)$ is limited by $C_\mu^* = \max(C_\mu^*, 0.0005)$. The nominal level for C_μ^* in a zero-pressure-gradient log layer is approximately 0.09.

Other parameters are given by

$$\eta^2 \equiv \{\mathbf{S}^2\} = S_{ij}S_{ji} = S_{ij}S_{ij} \tag{27}$$

$$\{\mathbf{W}^2\} = W_{ij}W_{ji} = -W_{ij}W_{ij} \tag{28}$$

$$\mathcal{R}^2 = -\frac{\{\mathbf{W}^2\}}{\{\mathbf{S}^2\}} \tag{29}$$

$$a_1 = \frac{1}{2}\left(\frac{4}{3} - C_2\right) \tag{30}$$

$$a_2 = \frac{1}{2}\left(2 - C_4\right) \tag{31}$$

$$a_3 = \frac{1}{2}\left(2 - C_3\right) \tag{32}$$

$$a_4 = \left[\gamma_1^* - 2\gamma_0^*\left(\frac{\alpha_1}{\tau}\right)\eta^2\tau^2\right]^{-1}\tau. \tag{33}$$

Also,

$$\gamma_0^* = C_1^1/2 \tag{34}$$

$$\gamma_1^* = \frac{1}{2}C_1^0 + \left(\frac{C_{\varepsilon 2} - C_{\varepsilon 1}}{C_{\varepsilon 1} - 1}\right) \tag{35}$$

and $C_{\varepsilon 1} = 1.44$, $C_{\varepsilon 2} = 1.83$, $C_1^0 = 3.4$, $C_1^1 = 1.8$, $C_2 = 0.36$, $C_3 = 1.25$, and $C_4 = 0.4$.

The above implementation is exactly the same for EASM(K-ω) or EASM(K-ε), except that $\tau \equiv K/\varepsilon$ for EASM(K-ε). However, the models are different with regard to the two-equation model to which they are coupled. For EASM(K-ω), the explicit tensor representation for τ_{ij} is coupled with the following K-ω two-equation model:

$$\frac{DK}{Dt} = \mathcal{P} - f_{\beta^*}K\omega + \frac{\partial}{\partial x_k}\left[\left(\nu + \frac{\nu_t^*}{\sigma_K}\right)\frac{\partial K}{\partial x_k}\right] \tag{36}$$

$$\frac{D\omega}{Dt} = \gamma\frac{\omega}{K}\mathcal{P} - \beta\omega^2 + \frac{\partial}{\partial x_k}\left[\left(\nu + \frac{\nu_t^*}{\sigma_\omega}\right)\frac{\partial \omega}{\partial x_k}\right], \tag{37}$$

where

$$\mathcal{P} = -\tau_{ij}\frac{\partial u_i}{\partial x_j} \approx 2\nu_t^*\eta^2 \tag{38}$$

and $\sigma_K = 2$, $\sigma_\omega = \kappa^2/[\sqrt{C_\mu}(\beta-\gamma)]$, $\kappa = 0.41$, $\gamma = 0.575$, $\beta = 0.83$, and $C_\mu = 0.0895$. Note that for 2-D incompressible flows, $\mathcal{P} = 2\nu_t^*\eta^2$ is exact. In the current implementation, $\mathcal{P}$ in the K-equation is limited to be less than 20 times the destruction term $f_{\beta^*}K\omega$. The function f_{β^*} from Wilcox[22] improves the performance of the K-ω model for 2-D shear layers, wakes, and jets and is given by

$$f_{\beta^*} = 1 \quad \text{when} \quad \chi_k \le 0 \tag{39}$$

$$f_{\beta^*} = \frac{1+680\chi_k^2}{1+400\chi_k^2} \quad \text{when} \quad \chi_k > 0 \tag{40}$$

$$\chi_k = \frac{C_\mu^2}{\omega^3}\frac{\partial K}{\partial x_j}\frac{\partial \omega}{\partial x_j}, \tag{41}$$

where the C_μ^2 term in the formula for χ_k is necessary because ω in the current model does not "absorb" C_μ as in Wilcox's model.

The boundary conditions applied at solid walls are $K_w = 0$ and $\omega_w = 10(6\nu_w)/[\beta(\Delta n)^2]$, where Δn is the distance to the first cell center away from the wall. The boundary condition for ω_w is from Menter.[5] This boundary condition simulates the analytical behavior of ω near solid walls without the need for specifying the solution at interior points.

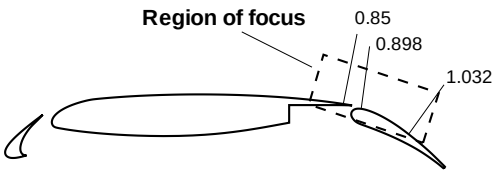

Figure 1. The 30P-30N multielement configuration.

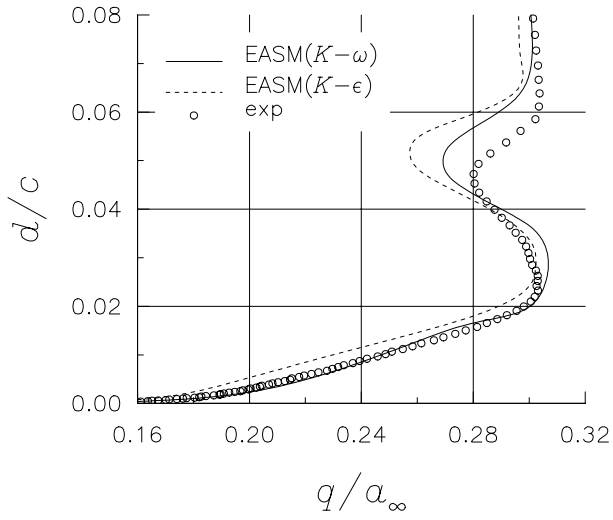

Figure 2. Velocity profiles near trailing edge of main element at $x/c = 0.85$.

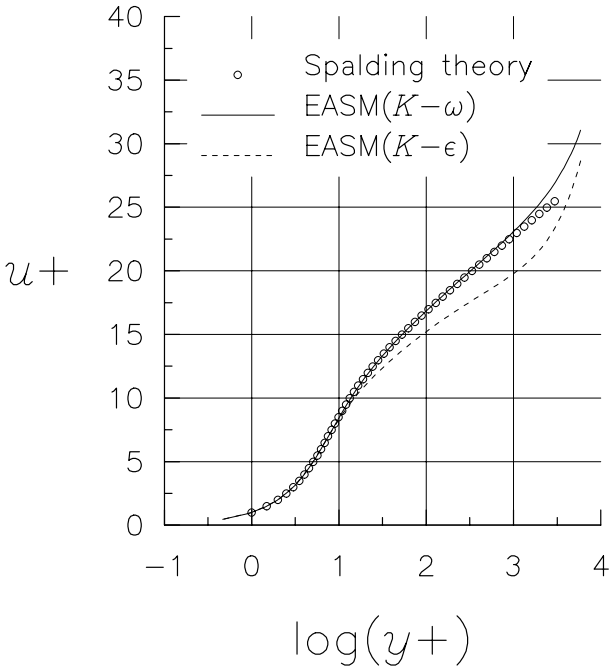

Figure 3. Velocity profiles in wall variables at $x/c = 0.85$.

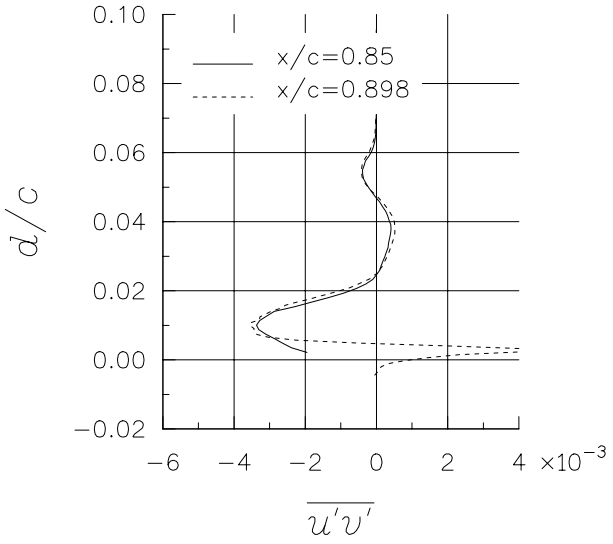

Figure 4. Experimentally measured turbulent shear stress at two locations near the main element trailing edge (dashed curve shifted down by 0.007 units).

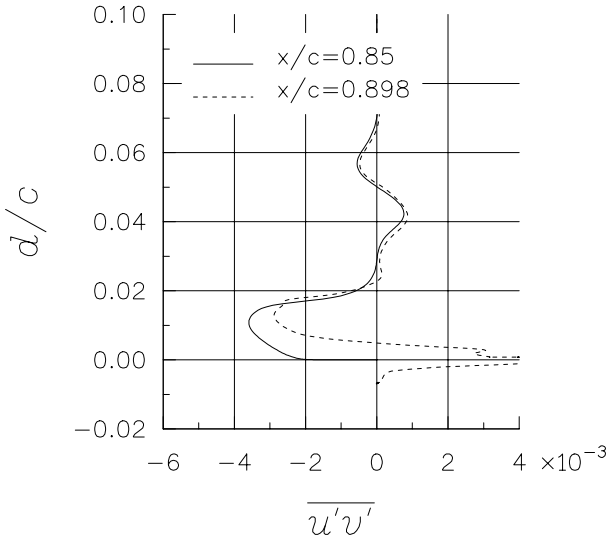

Figure 6. The EASM turbulent shear stress at two locations near the main element trailing edge (dashed curve shifted down by 0.007 units).

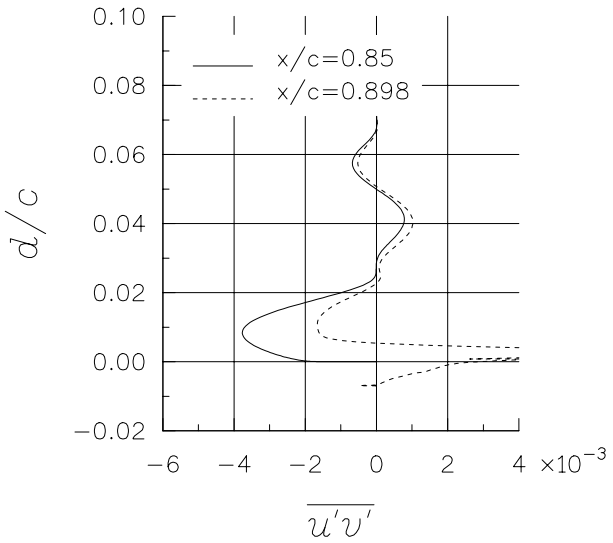

Figure 5. The SA model turbulent shear stress at two locations near the main element trailing edge (dashed curve shifted down by 0.007 units).

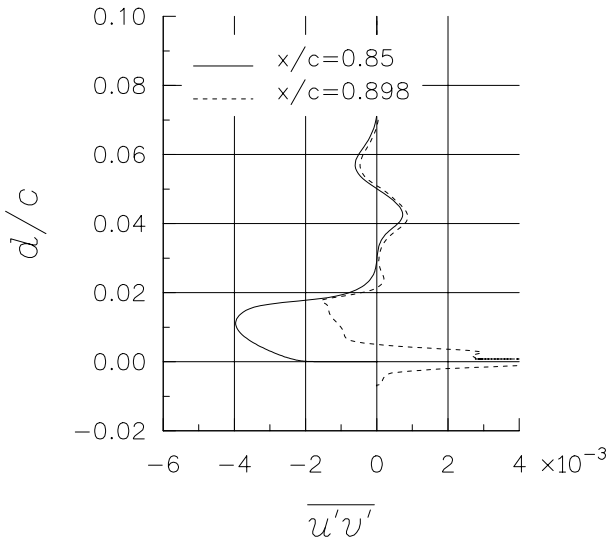

Figure 7. Linear EASM turbulent shear stress at two locations near the main element trailing edge (dashed curve shifted down by 0.007 units).

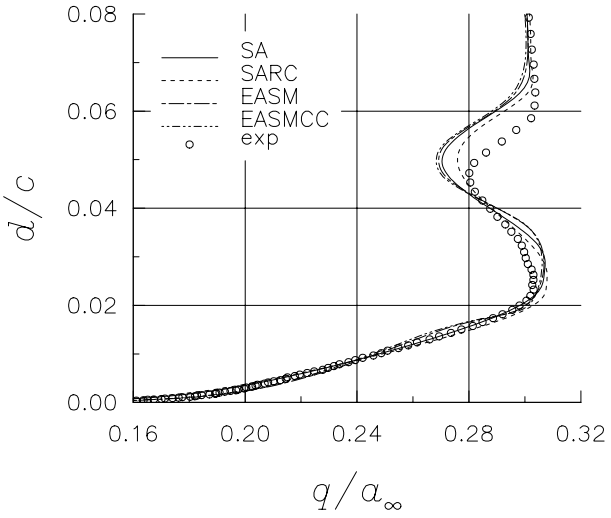

Figure 8. Velocity profiles near trailing edge of main element at $x/c = 0.85$.

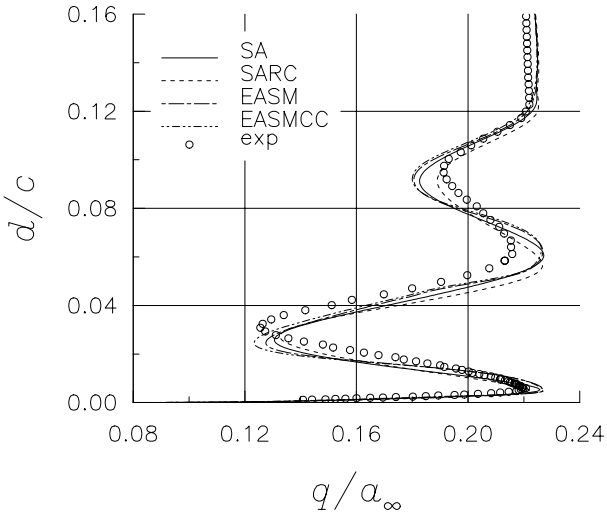

Figure 10. Velocity profiles near midflap at $x/c = 1.032$.

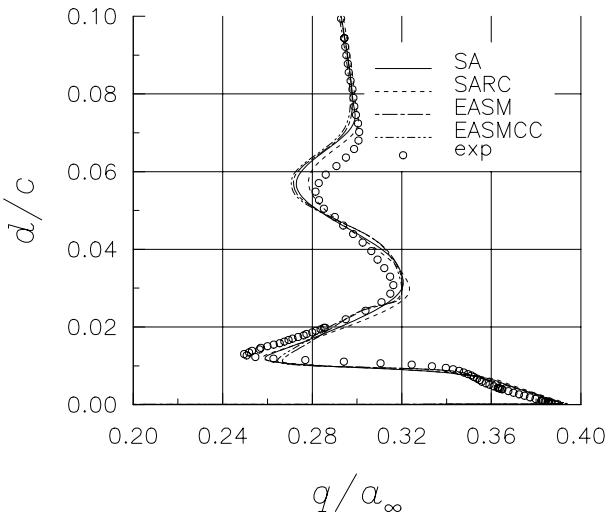

Figure 9. Velocity profiles on flap just downstream of main element at $x/c = 0.898$.

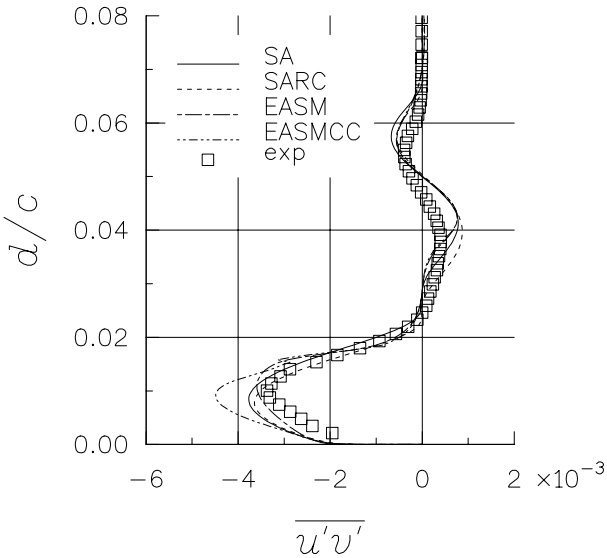

Figure 11. Turbulent shear stress profiles near trailing edge of main element at $x/c = 0.85$.

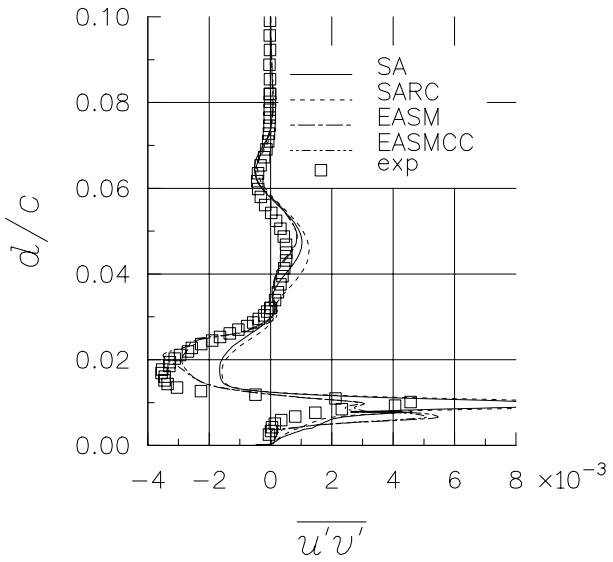

Figure 12. Turbulent shear stress profiles on flap just downstream of main element at $x/c = 0.898$.

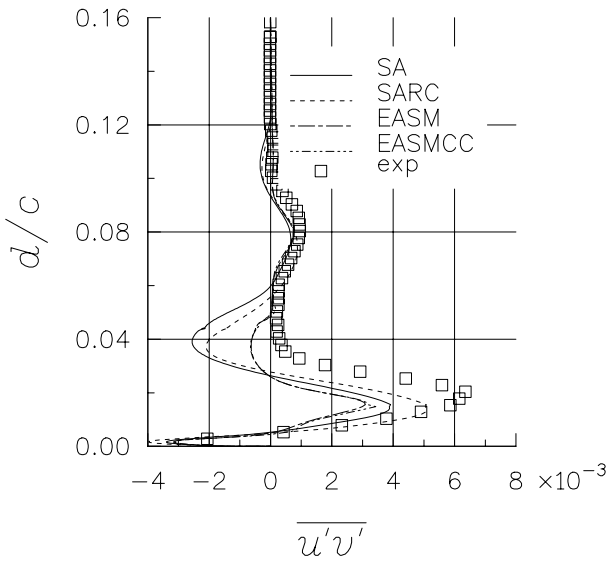

Figure 13. Turbulent shear stress profiles near mid-flap at $x/c = 1.032$.

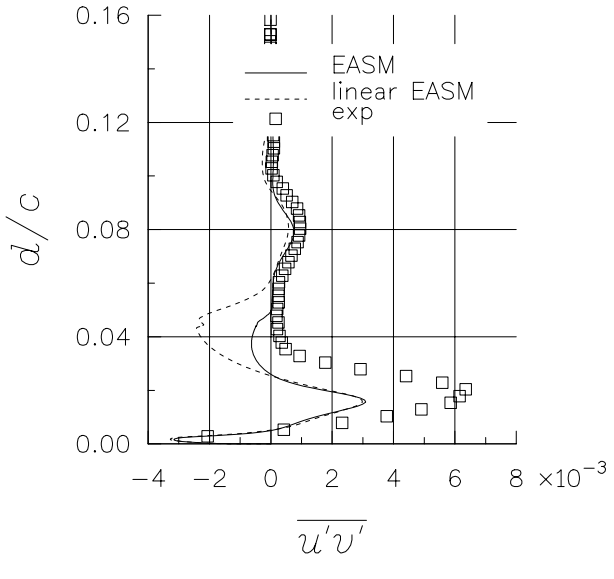

Figure 14. Effect of nonlinear terms on turbulent shear stress profiles at $x/c = 1.032$.

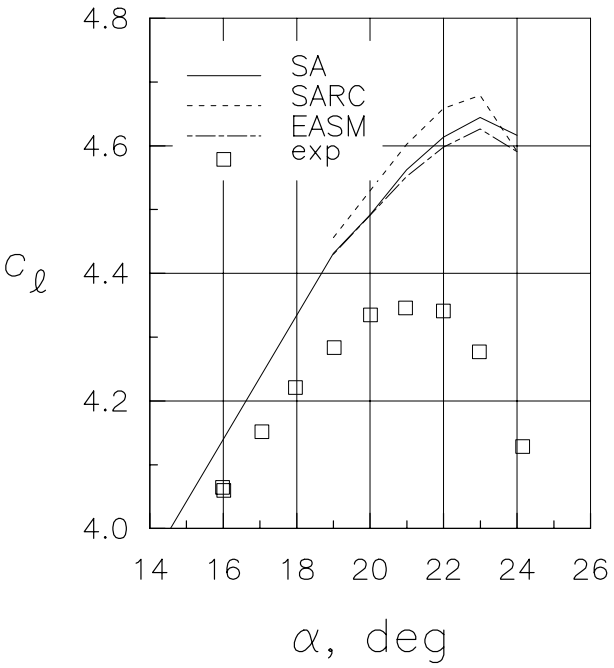

Figure 15. Lift coefficients near maximum lift.